Annals of Biomedical Engineering, Vol. 28, pp. 1218–1228, 2000
Printed in the USA.

0090-6964/2000/28(10)/1218/11/$15.00

Current Distribution in Skeletal Muscle Activated by Functional Electrical Stimulation: Image-Series Formulation and Isometric Recruitment Curve

L. M. LIVSHITZ,[1] P. D. EINZIGER,[2] and J. MIZRAHI[1]

Departments of [1]Biomedical and [2]Electrical Engineering, Technion, Israel Institute of Technology, Haifa 32000, Israel

(Received 24 December 1998; accepted 6 September 2000)

Abstract—The present work develops an analytical model that allows one to estimate the current distribution within the whole muscle and the resulting isometric recruitment curve (IRC). The quasistatic current distribution, expressed as an image series, i.e., a collection of properly weighted and shifted point-source responses, outlines an extension for more than three layers of the classical image theory in conductive plane-stratified media. Evaluation of the current distribution via the image series expansions requires substantially less computational time than the standard integral representation. The expansions use a unique recursive representation for Green's function, that is a generic characteristic of the stratification. This approach permits one to verify which of the tissue electrical properties are responsible for the current density distribution within the muscle, and how significant their combinations are. In addition, the model permits one to study the effect of different electrode placement on the shape and the magnitude of the potential distribution. A simple IRC model was used for parameter estimation and model verification by comparison with experimentally obtained isometric recruitment curves. Sensitivity of the model to different parameters such as conductivity of the tissues and activation threshold was verified. The resulting model demonstrated characteristic features that were similar to those of experimentally obtained data. The model also quantitatively confirmed the differences existing between surface (transcutaneous) and implanted (percutaneous) electrode stimulation. © *2000 Biomedical Engineering Society.* [S0090-6964(00)01110-3]

Keywords—Functional electrical stimulation, Nonhomogeneous medium, Green's function, Current distribution, Image series, Volume conductor, Isometric recruitment curve (IRC).

INTRODUCTION

In functional electrical stimulation (FES) we need to control the externally stimulated muscle to produce a desired output. Knowledge of the electric field distribution within the muscle is essential in determining which parts of the muscle have been excited and therefore take part in the force generation process. Thus, efficient procedures for the computation of the potential and the current density distributions in an artificially stimulated skeletal muscle with arbitrary placement of electrodes, surface or intramuscular, are necessary.

Significant differences in stimulus parameters and patterns of excitation were reported between intramuscular and surface stimulation electrodes.[4] Experimental studies suggest that, to elicit a functional muscle contraction of the quadriceps muscle by intramuscular electrodes, a regulated current of the order of 20 mA is sufficient,[1] whereas by surface electrodes a current of approximately 100 mA current is required.[26]

The difficulties encountered in applying field theory to biological tissues include their heterogeneity, anisotropy, and frequency-dependency of their electrical properties.[7] Fortunately, most FES applications involve currents with significant frequency components well below 10 kHz.[28] Under this condition, it is sufficient to deal with the stationary current in the quasistatic limit, which considerably simplifies the representation of the potential field and the resultant current distribution.

Modeling of whole-muscle excitation by external stimulation is a complex problem necessitating several simplifying assumptions. During FES of paraplegic patients, we stimulate large and powerful leg muscles.[1,21] Under this condition, the thigh can be approximated as a multilayered medium, where the skin, fat, and muscle are represented as flat, infinitely extended layers (e.g., Ref. 12).

A potentially promising approach is the use of the method known as the image technique (e.g., Ref. 36), expressing the potential distribution as a collection of properly weighted and shifted point-source responses.[15,17] The method of images is well known and has been extensively applied in the past in geophysical problems to solve the potential generated by a point source electrode in plane-layered media.[34,38] Grill[12] and Stegeman *et al.*,[35] used the image technique for the modeling of electric fields excited by point electrodes and active nerve bundles, respectively, in semi-infinite me-

Address correspondence to Professor J. Mizrahi, Dept. Biomedical Engineering, Technion, IIT, Haifa 32000, Israel. Electronic mail: jm@biomed.technion.ac.il

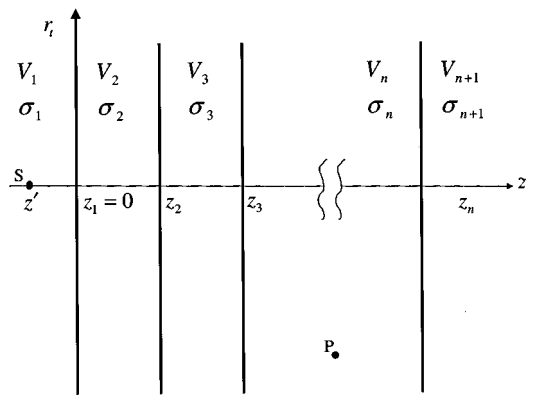

FIGURE 1. Physical configuration for conductive plane-stratified media, consisting of $n+1$ layers, with n boundaries between the layers. The observation point P, the source point S, and the transverse coordinate $\mathbf{r}_t$ are defined via: $\mathbf{r}=\mathbf{r}_t+z\hat{\mathbf{z}}=(x,y,z)$, $\mathbf{r}'=\mathbf{r}'_t+z'\hat{\mathbf{z}}=(0,0,z')$, and $\mathbf{r}_t=(x^2+y^2)^{1/2}$, respectively.

dium (i.e., a single plane boundary). Unfortunately, closed-form analytical expressions have not been derived for cases exceeding three layers.[18] Thus, an extension to a physical configuration containing more than three layers is essential for the utilization of the image technique in realistic problems.

In the present study, the classical image theory is extended to incorporate explicit image series expressions for plane-stratified media containing more than three layers. First, an integral representation for Green's function is introduced via a recursive construction of the reflection and transmission coefficients. Next, the Green's function is expanded in an infinite image series expansion and explicitly constructed for $n\leqslant 3$, utilizing these unique recursive relations which are a generic characteristic of the stratification. This analytical approach leads to an efficient procedure for the computation of the potential and the current density distributions in an artificially stimulated skeletal muscle with an arbitrary placement of surface or intramuscular electrodes. The method of images is the quasistatic limit of a wave phenomenon. Thus, we make use of wave analogy with its corresponding terminology, including reflection and transmission up to this limit.[6,15,17] A simple model is used for parameter estimation and model verification of the isometric recruitment curves (IRC), by comparison with experimentally obtained data.

QUASISTATIC FIELDS IN PLANE-STRATIFIED MEDIA

Physical Configuration

The physical configuration of our problem, depicted in Fig. 1, consists of a source-point S, an observation point P, and $n+1$ layers, with n boundaries between the layers (e.g., Refs. 14 and 27).

Green's Function

The current density $\mathbf{j}$ in the isotropic conductive media is linearly related to the electric field $\mathbf{E}$

$$\mathbf{j}=\sigma\mathbf{E}. \tag{1}$$

The quasistatic electric field $\mathbf{E}$ is conservative and thus can be expressed as the gradient of a scalar potential function V

$$\mathbf{E}=-\nabla V, \tag{2}$$

$$\nabla^2 V=-\frac{I}{\sigma}\delta(\mathbf{r}-\mathbf{r}'), \tag{3}$$

where $\mathbf{r}'=(0,0,z')$ and $\mathbf{r}=(x,y,z)$ are locations of the source-point S and the observation P point, respectively. I is the stimulation current, and σ is the piecewise constant isotropic conductivity of the medium. Evidently, the function V, known as Green's function, is a solution of Poisson's Eq. (3), and satisfies the following conditions:

$$\lim_{r\to\infty} rV<\infty, \tag{4}$$

$$V_{i+1}(\mathbf{r}_i)=V_i(\mathbf{r}_i), \tag{5}$$

$$\sigma_{i+1}\frac{\partial V_{i+1}(\mathbf{r}_i)}{\partial z}=\sigma_i\frac{\partial V_i(\mathbf{r}_i)}{\partial z}, \tag{6}$$

where $\mathbf{r}_i=(x,y,z_i)$, $i=1,2,...,n$.

Integral Representation

The solution of (3) for the configuration depicted in Fig. 1, and satisfying (4), (5), and (6), can be obtained via separation of variables, leading to Bessel's integral representation (e.g., Refs. 6, 17, and 38)

$$V_i(z,r_t)=\alpha\int_0^\infty\left[\prod_{j=1}^{i}T_j(\lambda)\right][e^{-\lambda|z-z'|}+R_i(\lambda)e^{\lambda(z+z')}]J_0(\lambda r_t)d\lambda,$$

$$z_{i-1}<z<z_i,\quad \alpha=I/4\pi\sigma_1, \tag{7}$$

where J_0 is the Bessel function of the first kind and order zero, $z_0=-\infty$, $z_{n+1}=-\infty$, and $i=1,2,...,n+1$;

$$R_i(\lambda)=\frac{K_i+R_{i+1}(\lambda)e^{2\lambda z_i}}{1+K_iR_{i+1}(\lambda)e^{2\lambda z_i}}e^{-2\lambda z_i},\quad R_{n+1}(\lambda)=0, \tag{8}$$

$$T_i(\lambda)=\frac{1+K_{i-1}}{1+K_{i-1}R_i(\lambda)e^{2\lambda z_{i-1}}}, \tag{9}$$

and

$$K_i=\frac{\sigma_i-\sigma_{i+1}}{\sigma_i+\sigma_{i+1}},\quad K_0=0. \tag{10}$$

The functions $R_i(\lambda)$ and $T_i(\lambda)$ represent the global reflection and transmission coefficients, respectively, whereas K_i denotes the (λ independent) local reflection coefficient of the ith interface. The representation of the integrand in (7) in terms of $R_i(\lambda)$ and $T_i(\lambda)$ constitutes an unique recursive construction via the intrinsic reflection coefficient K_i in (10). This form and its benefits has been overlooked in previous investigations (e.g., Refs. 17 and 18).

Numerical evaluation of the potential integral (7), for a prescribed set of observation points P (Fig. 1), requires massive computations. This may occur in particular, when (7) has to be evaluated repeatedly in a numerical algorithm, such as the solution of a three-dimensional potential problem for many mesh points. Thus, the image series expansion, introduced in the next section via the recursive relations in (8) and (9), is promising in obtaining an easy to implement and fast converging alternative representation for (7).

The Image Series Expansion

The integral in (7) can be expanded into a series of point-source responses also known as either Green's functions or image sources. The point-source responses are properly weighted and shifted, to satisfy (4), (5), and (6). The classical image series representation carried out for $n=1$ and $n=2$ (e.g., Refs. 15 and 36), where $n+1$ represents the number of layers depicted in Fig. 1, is extended herein to include $n=3$ which is essential for the FES problem discussed next. A model of the order of $n=3$ actually consists of four layers namely, air, skin, fat, and muscle. The classical expansions for $n=1$ or $n=2$ result in reduced forms, i.e., a two-term representation or a geometric series expansion, respectively. However, the case of $n=3$, expressed as geometric series followed by a binomial series, is quite general and outlines the expansion procedure for $n>3$ without any increase in the complexity.[23] In discussing the image series representations both for $n=1,2$, as reference solution,

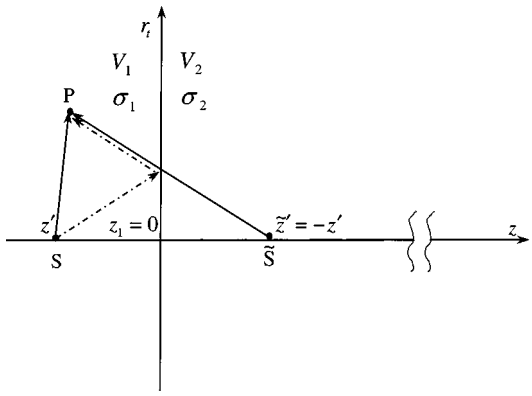

FIGURE 2. Physical configuration for a semiinfinite medium, $n=1$. Both contributions from the point-source S at $\mathbf{r}'=(0,0,z')$ and the image-source $\tilde{S}$ at $\tilde{\mathbf{r}}'=(0,0,\tilde{z}')=-\mathbf{r}'=(0,0,-z')$ reach the observation point P. The image-source ($\tilde{S}$) contribution (solid line) can be interpreted as the point-source (S) contribution undergoing a single reflection (K_1) at $z=z_1=0$ (dashdot line).

and for $n=3$, and to establish the general expansion procedure, we make use of the Weber–Lipschitz integral identity[36]

$$\int_0^\infty e^{-\lambda|z|}J_0(\lambda r_t)d\lambda=(r_t^2+z^2)^{-1/2}, \tag{11}$$

which is a vital tool in converting the integral representation (7) into an image series. For illustration, we present here image series expansions, when the source point is placed in the uppermost layer and the observation point is located in either the uppermost or in the lowermost layer.

Semiinfinite Medium, $n=1$. The physical configuration for $n=1$ is depicted in Fig. 2. Equations (8), (9), and (10) can be rewritten explicitly as

$$R_1(\lambda)=K_1, \tag{12}$$

$$T_1(\lambda)=1,\quad T_2(\lambda)=1+K_1, \tag{13}$$

and

$$K_1=\frac{\sigma_1-\sigma_2}{\sigma_1+\sigma_2}, \tag{14}$$

respectively. Then, utilizing (7) in conjunction with (11), one obtains

$$V_1=\alpha(1/D+K_1/\tilde{D}),\quad z<z_1=0, \tag{15}$$

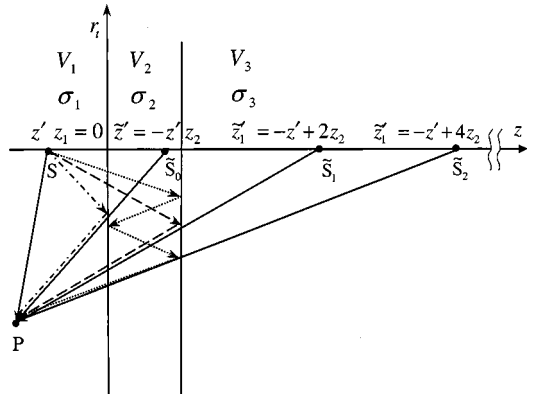

FIGURE 3. Physical configuration for a single conductive slab, $n=2$. Both contributions from the point sources S at $\mathbf{r}'=(0,0,z')$ and the image-source set $\tilde{S}_m^{(1)}$ at $\tilde{\mathbf{r}}_m'^{(1)}=(0,0,-\tilde{z}'+2mz_2)$ $(m=0,1,2,\ldots\tilde{S}_0^{(1)}=\tilde{S})$ reach the observation point P. The image-source set $(\tilde{S}_m^{(1)})$ contribution (solid line) can be interpreted as a point-source (S) contribution undergoing, at $z=z_1=0$, either a single refection (K_1, dash–dot line, $m=0$) or a single transmission in $(1+K_1)$ and out $(1-k_1)$ accompanied by single reflection (K_2) at $z=z_2$ and $m-1$ $(m\geq 1)$ bounces both at $z_1((-K_1)^{m-1})$ and z_2 $(K_2^{m-1}$, dashed and dotted lines for $m=1$ and $m=2$, respectively).

$$V_2=\alpha(1+K_1)/D,\quad 0=z_1<z, \tag{16}$$

where (Fig. 2),

$$D=|\mathbf{r}-\mathbf{r}'|=[r_t^2+(z-z')^2]^{1/2}, \tag{17}$$

$$\tilde{D}=|\mathbf{r}-\tilde{\mathbf{r}}'|=[r_t^2+(z+z')^2]^{1/2},\quad \tilde{\mathbf{r}}'=-\mathbf{r}'. \tag{18}$$

As depicted in Fig. 2, both contributions from the point-source at $\mathbf{r}'=(0,0,z')$ and the image source at $\tilde{\mathbf{r}}'=-\mathbf{r}'=(0,0,\tilde{z}')=(0,0,-z')$ reach the observation point P. The image-source contribution can be interpreted as the point-source contribution undergoing a single reflection (K_1) at $z=z_1=0$. Similarly, the point-source contribution, reaching an observation point lying in the half-space $z>0$ [Eq. (16)], can be interpreted as undergoing a single transmission $(1+K_1)$ at $z=z_1=0$. Note that expressions (15) and (16) are similar to previously published results (e.g., Refs. 15 and 36).

Three Layers, $n=2$. The physical configuration for a single conductive slab is depicted in Fig. 3. Equations (8), (9), and (10) can be expressed as

$$R_1(\lambda)=K_1+\frac{(1-K_1^2)R_2(\lambda)}{1+K_1R_2(\lambda)},\quad R_2(\lambda)=K_2e^{-2\lambda z_2}, \tag{19}$$

$$T_1(\lambda)=1,\quad T_2(\lambda)=\frac{1+K_1}{1+K_1R_2(\lambda)},\quad T_3(\lambda)=1+K_2, \tag{20}$$

and

$$K_1=\frac{\sigma_1-\sigma_2}{\sigma_1+\sigma_2},\quad K_2=\frac{\sigma_2-\sigma_3}{\sigma_2+\sigma_3}, \tag{21}$$

respectively. Expanding $R_1(\lambda)$ in Eq. (19) into a geometric series [in $K_1R_2(\lambda)$] and then utilizing (7) in conjunction with (11), results in

$$V_1=\alpha\left[1/D+K_1/\tilde{D}+K_2(1-K_1^2)\times\sum_{m=1}^{\infty}(-K_1K_2)^{m-1}/\tilde{D}_m^{(1)}\right],\quad z<z_1=0. \tag{22}$$

Similarly, a geometric series expansion of $T_2(\lambda)$ in Eq. (20) results in

$$V_3=\alpha(1+K_1)(1+K_2)\sum_{m=0}^{\infty}(-K_1K_2)^m/\tilde{D}_m^{(2)},\quad z_2<z, \tag{23}$$

where D and $\tilde{D}$ are given in (17) and (18), respectively, and

$$\tilde{D}_m^{(2)(1)}=|\mathbf{r}-\tilde{\mathbf{r}}_m'^{(2)(1)}|=\{r_t^2+[z-\tilde{z}_m'^{(2)(1)}]^2\}^{1/2}, \tag{24}$$

$$\tilde{\mathbf{r}}_m'^{(2)(1)}=[0,0,\tilde{z}_m'^{(2)(1)}],\quad \tilde{z}_m'^{(2)(1)}=\mp(z'-2mz_2). \tag{25}$$

Note that $\tilde{D}_0^{(1)}=\tilde{D}F(\tilde{\mathbf{r}}_0'^{(1)}=\tilde{\mathbf{r}}'=-\mathbf{r}')$ and $\tilde{D}_0^{(2)}=DF(\tilde{\mathbf{r}}_0'^{(2)}=\mathbf{r}')$.

As depicted in Fig. 3, both contributions from the point sources at $\mathbf{r}'=(0,0,z')$ and the image-source set located at $\tilde{\mathbf{r}}_m'^{(1)}$ [Eq. (25)] reach the observation point **P**. The contribution of the image-source set [Eq. (22)] can be interpreted as a summation, over all the point-source responses undergoing at $z=z_1=0$, either a single reflection $(K_1, m=0)$ or a single transmission in $(1+K_1)$ and out $(1-K_1)$ accompanied by single reflection (K_2) at $z=z_2$ and $m-1$ $(m\geq 1)$ bounces both at $z_1F[(-K_1)^{m-1}]$ and $z_2F(K_2^{m-1})$. Similarly, contribution from the image-source set $[\tilde{\mathbf{r}}_m'^{(2)}$, in Eq. (25)], reaching an observation point lying in the half space $z>z_2$ [Eq. (23)], can be interpreted as a summation over all the point-source responses undergoing two successive transmissions $(1+K_1)$ and $(1+K_2)$ and m bounces

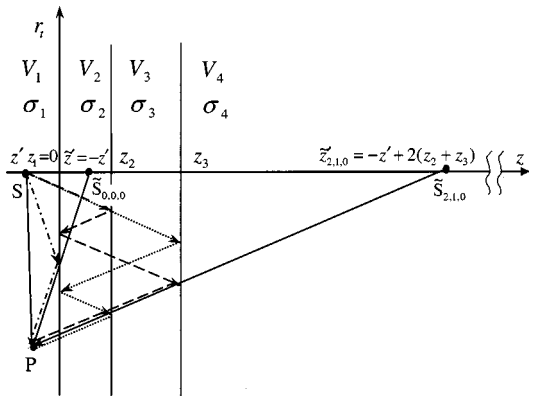

FIGURE 4. Physical configuration for a double slab geometry, $n=3$. Both contributions from the point sources S at $\mathbf{r}'=(0,0,z')$ and the image-source set $\tilde{S}^{(1)}_{m_1,l,m_2}$ at $\tilde{\mathbf{r}}'^{(1)}_{m_1,l,m_2}=[0,0,-\tilde{z}'+2m_1z_2+2(m_1-l+m_2)(z_3-z_2)]$ $(m_1=0,1,2,\ldots;l=0,1,\ldots,m_1;m_2=0,1,2,\ldots;\tilde{S}^{(1)}_{0,0,0}=\tilde{S})$ reach the observation point P. The image-source set $(\tilde{S}^{(1)}_{m_1,l,m_2})$ contribution (solid line) can be interpreted as a point-source (S) contribution undergoing, at $z=z_1=0$, either a single reflection (K_1, dash-dot line, $m_1=0$) or a single transmission in $(1+K_1)$ and out $(1-K_1)$, accompanied by all possible combinations of bounces and transmissions at $z=z_1=0$, $z=z_2$ and $z=z_3$, $\binom{m_1}{l}\binom{m_1-l+m_2-1}{m_2}$, where $m_1-1(m_1\geq 1)$ and m_2 denote the number of internal reflections at $z=z_1=0$ $[(-K_1)^{m_1-1}]$ and $z=z_2$ $[(-K_2)^{m_2}]$, respectively, and m_1-l is the number of transmission in $(1+K_2)$ and out $(1-K_2)$ at $z=z_2$ $[(m_1,l,m_2)=(2,1,0)]$ associated with the two only combinations depicted by dashed and dotted lines.

$[(-K_1)^m$ and $K_2^m]$ both at z_1 and z_2, respectively. The image series expansion in (22) and (23) converges if at least one of $|K_1|$, $|K_2|$ is less than unity.[15] Note that expression (22) is similar to previously published results (e.g., Refs. 15 and 36).

Four Layers, $n=3$. The physical configuration for double slab geometry is depicted in Fig. 4. Equations (8), (9), and (10) can be reduced into

$$R_1(\lambda)=K_1+\frac{(1-K_1^2)R_2(\lambda)}{1+K_1R_2(\lambda)},$$

$$R_2(\lambda)=K_2e^{-2\lambda z_2}+\frac{(1-K_2^2)R_3(\lambda)}{1+K_2R_3(\lambda)e^{2\lambda z_2}},$$

$$R_3(\lambda)=K_3e^{-2\lambda z_3}, \tag{26}$$

$$T_1(\lambda)=1,\quad T_2(\lambda)=\frac{1+K_1}{1+K_1R_2(\lambda)},$$

$$T_3(\lambda)=\frac{1+K_2}{1+K_2R_3(\lambda)e^{2\lambda z_2}},\quad T_4(\lambda)=1+K_3, \tag{27}$$

and

$$K_1=\frac{\sigma_1-\sigma_2}{\sigma_1+\sigma_2},\quad K_2=\frac{\sigma_2-\sigma_3}{\sigma_2+\sigma_3},\quad K_3=\frac{\sigma_3-\sigma_4}{\sigma_3+\sigma_4}, \tag{28}$$

respectively. We refer to Eq. (26) and, as previously, expand $R_1(\lambda)$ into a geometric series [in $K_1R_2(\lambda)$] followed by a binomial series for $R_2(\lambda)$ [in $K_2R_3(\lambda)$]. Then, using Eq. (7) in conjunction with Eq. (11), results in

$$\begin{aligned}V_1=\alpha\Bigg[&1/D+K_1/\tilde{D}+(1-K_1^2)\\&\times\sum_{m_1=1}^{\infty}(-K_1)^{m_1-1}\sum_{l=0}^{m_1}\binom{m_1}{l}\\&\times K_2^l[(1-K_2^2)K_3]^{m_1-l}\sum_{m_2=0}^{\infty}\binom{m_1-l+m_2-1}{m_2}\\&\times(-K_2K_3)^{m_2}/\tilde{D}^{(1)}_{m_1,l,m_2}\Bigg],\quad z<z_1=0.\end{aligned} \tag{29}$$

Similarly, expanding $T_2(\lambda)$ in Eq. (27) into a geometric series, followed by a binomial series expansion for $R_2(\lambda)$, results in

$$\begin{aligned}V_4=a\prod_{i=1}^{3}(1+K_i)&\sum_{m_1=0}^{\infty}(-K_1)^{m_1}\\&\times\sum_{l=0}^{m_1}\binom{m_1}{l}K_2^l[(1-K_2^2)K_3]^{m_1-l}\sum_{m_2=0}^{\infty}\binom{m_1-l+m_2}{m_2}\\&\times(-K_2K_3)^{m_2}/\tilde{D}^{(2)}_{m_1,l,m_2},\quad z_3<z\end{aligned} \tag{30}$$

where D and $\tilde{D}$ are given in (17) and (18), respectively, and

$$\tilde{D}^{(1)}_{(2)\,m_1,l,m_2}=|\mathbf{r}-\tilde{\mathbf{r}}'^{(1)}_{(2)\,m_1,l,m_2}|=\{r_t^2+[z-\tilde{z}'^{(1)}_{(2)\,m_1,l,m_2}]^2\}^{1/2}, \tag{31}$$

$$\tilde{\mathbf{r}}'^{(1)}_{(2)\,m_1,l,m_2}=[0,0,\tilde{z}'^{(1)}_{(2)\,m_1,l,m_2}],$$

$$\tilde{z}'^{(1)}_{(2)\,m_1,l,m_2}=\mp[z'-2m_1z_2-2(m_1-l+m_2)(z_3-z_2)]. \tag{32}$$

Note that $\tilde{D}^{(1)}_{0,0,0}=\tilde{D}[\tilde{\mathbf{r}}'^{(1)}_{0,0,0}=\tilde{\mathbf{r}}'=-\mathbf{r}']$ and $\tilde{D}^{(2)}_{0,0,0}=D$ $[\tilde{\mathbf{r}}'^{(2)}_{0,0,0}=\mathbf{r}']$.

As depicted in Fig. 4, both contributions from the point-sources S at $\mathbf{r}'$ and the image-source set at $\tilde{\mathbf{r}}'^{(1)}_{m_1,l,m_2}$ [Eq. (32)] reach the observation point $\mathbf{P}$. The contribution of the image-source set Eq. (29) can be interpreted as a summation over all the point-source responses undergoing, at $z=z_1=0$, either a single reflection $(K_1, m_1=0)$ or a single transmission in $(1+K_1)$ and out $(1-K_1)$, accompanied by all possible combinations of bounces and transmissions at $z=z_1=0$, $z=z_2$, and $z=z_3$, $\binom{m_1}{l}\binom{m_1-l+m_2-1}{m_2}$. Here $m_1-1 (m_1 \geq 1)$ and m_2 denote the number of internal reflections at z_1 $[(-K_1)^{m_1-1}]$ and z_2 $[(-K_2)^{m_2}]$, respectively, and m_1-l is the number of transmission in $(1+K_2)$ and out $(1-K_2)$ at $z=z_2$. Similarly, contribution from the image-source set $[\tilde{\mathbf{r}}'^{(2)}_{m_1,l,m_2}$, in Eq. (32)] reaching an observation point lying in the half space $z>z_3$ [Eq. (30)], can be interpreted as a summation over all the point-source responses undergoing three successive transmissions $(1+K_1)$, $(1+K_2)$, and $(1+K_3)$ at z_1, z_2, and z_3, accompanied by all possible combinations of bounces and transmissions at $z=z_1=0$, $z=z_2$, and $z=z_3$, $\binom{m_1}{l}\times\binom{m_1-l+m_2}{m_2}$. Here m_1 and m_2 denote the number of internal reflections at z_1 $[(-K_1)^{m_1}]$ and z_2 $[(-K_2)^{m_2}]$, respectively, and m_1-l is the number of transmission in $(1+K_2)$ and out $(1-K_2)$ at z_2. The image series expansion in (29) and (30) converges if at least two of $|K_1|$, $|K_2|$, and $|K_3|$ are less than unity.[6]

VOLUME CONDUCTION FIELD MODEL

In this section, we apply (30) and (29) to the following two volume conductor field configurations: (a) transcutaneous (surface) stimulation and (b) percutaneous (intramuscular) stimulation.

Transcutaneous Model

Placing the stimulation electrode over the first interface $z'=0$ $(n=4)$, see Fig. 1, and modeling the upper-half space as an air layer, $\sigma_1=0$ $(K_1=-1)$, both the integral representation in (7) and the image series expansion in (30) are reduced to

$$V_4=\alpha_1\int_0^\infty \frac{(1+K_2)(1+K_3)e^{-\lambda z}}{[1-R_2(\lambda)][1+K_2R_3(\lambda)e^{2\lambda z_2}]} \times J_0(\lambda r)d\lambda,\quad a_1=I/2\pi\sigma_2,\quad z>z_3 \tag{33}$$

and

$$V_4=a_1\prod_{i=2}^{3}(1+K_i)\sum_{m_l=0}^{\infty}\sum_{l=0}^{m_1}\binom{m_1}{l} \times K_2^l[(1-K_2^2)K_3]^{m_1-l}\sum_{m_2=0}^{\infty}\binom{m_2+m_1-l}{m_2} \times(-K_2K_3)^{m_2}/\tilde{D}^{(2)}_{m_1,m_2,l}, \tag{34}$$

respectively. The parameters; σ_2, σ_3, and σ_4, in (28), denote the conductivities of the skin, fat, and muscle layers, respectively.

Percutaneous Model

Modeling the lower-half space as an air layer (Fig. 4), $\sigma_4=0$ $(K_3=1)$, both the integral representation in (7) and the image series expansion in (29) are reduced to

$$V_1=\alpha\int_0^\infty\left[e^{-\lambda|z-z'|}+K_1e^{(z+z')\lambda} + \frac{(1-K_1^2)R_2(\lambda)e^{\lambda(z+z')}}{1+K_1R_2(\lambda)}\right]J_0(\lambda r)d\lambda,\quad z<z_1=0 \tag{35}$$

and

$$V_1=\alpha\left[1/D+K_1/\tilde{D}+(1-K_1^2) \times\sum_{m_1=1}^{\infty}(-K_1)^{m_1-1}\sum_{l=0}^{m_1}\binom{m_1}{l} \times K_2^l(1-K_2^2)^{m_1-l}\sum_{m_2=0}^{\infty}\binom{m_1-l+m_2-l}{m_2} \times(-K_2)^{m_2}/\tilde{D}^{(1)}_{m_1,l,m_2}\right], \tag{36}$$

respectively, where $R_2(\lambda)$ in (26) takes the form

$$R_2(\lambda)=K_2e^{-2\lambda z_2}+\frac{(1-K_2^2)e^{-2\lambda z_3}}{1+K_2e^{-2\lambda(z_3-z_2)}}. \tag{37}$$

The parameters; σ_1, σ_2, and σ_3 in (28), denote the conductivities of the muscle, fat, and skin, respectively. Note that Eq. (35) is an alternative representation of that given by Stefanesco *et al.*[34] The study of a two-electrode model is accomplished by applying the superposition principle. The two electrodes namely the anode and the cathode are placed along the x axis. Both the anodal and

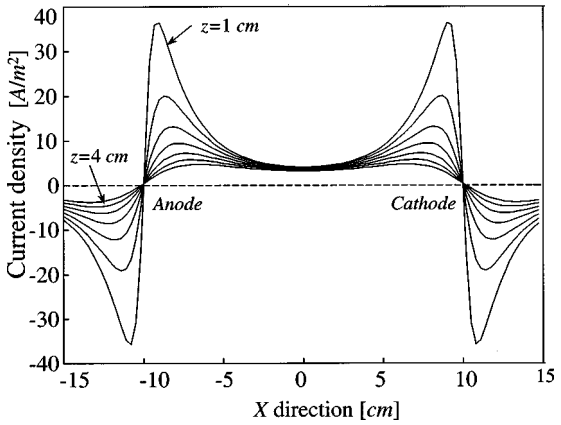

FIGURE 5. Variation of the *x* component of the current density with depth in the lowermost layer. The depth increment between the curves is 0.5 cm ($K_2=0.81$ and $K_3=-0.89$).

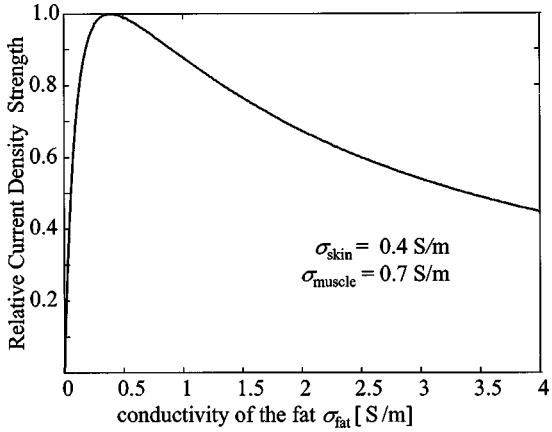

FIGURE 6. Influence of the conductivity of the fat layer on the current density.

cathodal currents have equal amplitudes but opposite directions.

MODEL SIMULATION AND VERIFICATION

Electric Field Simulation

For illustration, we present the numerical results for the transcutaneous model simulation. The criterion for the selection of these presented results was the relative importance of the stimulation parameters in potential practical FES applications. These included electric field distribution, skin and fat conductivities, and activation threshold. Both the numerical evaluations of the integrals and the image series calculation were implemented by using MATLAB 5.3 (MathWorks corp). For typical resistivity contrasts between the biological tissues ($|K|<0.9$), up to third order terms ($m_1=m_2=3$) in the series expansion (34) were found sufficient to obtain convergence within more than 95% of the exact solution. Using the image series technique, a computational time reduction of 30 fold was obtained compared to the numerical integration (subroutine *trapz* of aforementioned Matlab 5.3).

In all the model evaluations, the following parameters were used: interelectrode distance of 20 cm and thicknesses of the skin and fat were set to 0.4 and 0.6 cm, respectively. The mesh step used across the thickness of 0.1 cm was found numerically efficient, yet small enough to avoid discretization errors.

Typical conductivity values were as follows:[7] for skin $\sigma_{\text{skin}}=0.1-0.8$ S/m, and for the fat layer $\sigma_{\text{fat}}=0.04$ S/m. Muscle was assumed to be isotropic and the bulk conductivity values used for σ_{muscle} were in the range of 0.2–0.7 S/m. Due to the variability of the data found in the literature on the skin and muscle conductivity these quantities were subject to parameter estimation.

Figure 5 presents the variation of the *x* component of the current density with depth in the muscle layer within a plane perpendicular to the skin surface and passing through the point sources ($y=0$). The maximal stimulation current is 120 mA and each curve corresponds to a specific *z* level. The current density under the skin-electrode junction in the muscle layer is not uniform. It is highest in the area underneath the electrode where the input current is applied (40 A/m^2) and decreases rapidly further away from the electrode to (~4 A/m^2) and shows a near uniform electric field distribution midway between electrodes. The selected values for the reflection coefficients in Fig. 5, $K_2=0.81$ and $K_3=-0.89$, will be later justified in reporting on the optimal parameter estimation.

The influence of the conductivity of the intermediate (fat) layer on the current density distribution within the muscle slice in the transcutaneous model is shown in Fig. 6. In this graph the conductivity σ_{fat} was changed from 0 to 4 S/m, while the thickness of the layer was held constant. Increasing the conductivity of the intermediate layer leads to a decline of the current density within the lowermost layer. Variation of the distance from the current electrode shows a little effect on the current density value. It is obvious that if $\sigma_{\text{fat}}\approx 0$, no current can spread into the lowermost layer since the current pathway is totally restricted within the uppermost layer. While increasing the conductivity, the current density increases until it is maximum ($K_2\approx 0$, or $\sigma_{\text{skin}}\approx\sigma_{\text{fat}}$). However, further increasing of the conductivity leads to a shunt effect and the current density decreases.

Model Verification

For validation of the model, we used experimental isometric recruitment results from three paraplegic subjects from previous studies conducted by our group. The detailed procedures of the preparation of the subjects,

placement of the electrodes, and measurement protocols are as described in these studies.[20,25] Data indicating that the maximal force may be achieved by intramuscular stimulation of the quadriceps muscle at stimulus level of 20–30 mA were taken from the current literature.[4]

The IRC of a muscle is defined as the relation between the stimulus activation level and the output force when the muscle is held at a fixed length. The shape of the IRC during FES is determined, among various factors, by the electric field distribution, location, fiber size distribution of the excitable elements, and their excitation thresholds.[5] The activation threshold, which is a measure of the interaction between the external electric field and the excitable fibers, is a complex property that is in this study subject to parameter estimation using the experimentally obtained isometric recruitment curve.

There are several accepted mechanisms of fiber excitation.[3,16,24,29–33,40] The ''activation function'' proposed by Rattay,[30] relies on the second spatial longitudinal derivative of the external potential, and is valid for the case of infinitely long, straight, and uniform fibers. For other cases, namely, fiber termination, nonuniformity, curvature, etc., Roth[33] suggested that activation will most likely take place where the electric field, i.e., the first derivative of the potential is larger.

Figure 5 plots current density which is proportional to field strength. It shows a nearly uniform distribution in the deeper layers of the muscle, where the spatial derivative of the electric field is indeed near zero. Real shape, finite size electrode gives a uniform distribution.[23] Therefore there would, in theory, be zero net current transfer through the membrane. However, the field within the skeletal muscle is never uniform. Furthermore, an effective field gradient will result for any change in the axon conditions (e.g., diameter, direction, with respect to a locally uniform field), or if the axon is terminated in the field (as with free nerve endings, or nerve connections at muscle fibers). Consequently we used the electric field strength (or the linearly related current density) as the more appropriate activation threshold criterion for a uniform electric field as suggested by Reilly.[31,32]

In our work, the pulse duration was held constant (250 μs) and the amplitude of the stimulation was varied (0–120 A).[26] However, these two quantities are not mutually independent but are experimentally related to each other through the strength-duration curves (SDC).[31,39] Thus, the threshold can be scaled by means of the SDC to either pulse duration or amplitude. The effects of fiber diameter and electrode/fiber distance on the nerve activation threshold are also mutually dependent.[31] In our model since all the fibers are assumed identical, the activation threshold is a function of the fiber/electrode distance.

The force produced was calculated as the ratio of the number of active fibers to the overall number of fibers in the muscle. Although the muscle slice was represented as a semiinfinite (unbounded) layer in the four-layer model configuration, it was assumed that the layer is effectively bounded, i.e., that only a finite part of this slice could generate a force. The thickness, width and length of this active part were taken to be 3, 4, and 30 cm, respectively, and were based on magnetic resonance imaging (MRI) measurements made on paraplegic patients.[19]

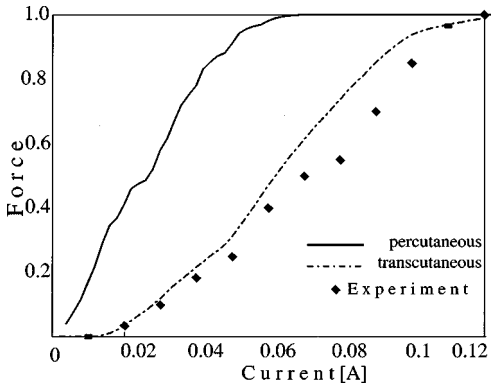

FIGURE 7. The IRC of the transcutaneous and percutaneous models.

The minimum root-mean-square error criterion between the experimental data and model solution was used to determine the best fit solution of the IRC problem for the transcutaneous model. Note that the obtained parameters had to also satisfy the percutaneous model for which saturation is reached at 40–50 mA. It should be noted, however, that percutaneous stimulation is limited to 30 mA approximately due to possible tissue damage near the stimulating electrode.

Figure 7 shows the IRC of the transcutaneous and the percutaneous models. The squared dots represent the experimental IRC of a paraplegic patient in transcutaneous stimulation. The current density threshold is held constant at 3.5 A/m^2. The intramuscular IRC has a higher

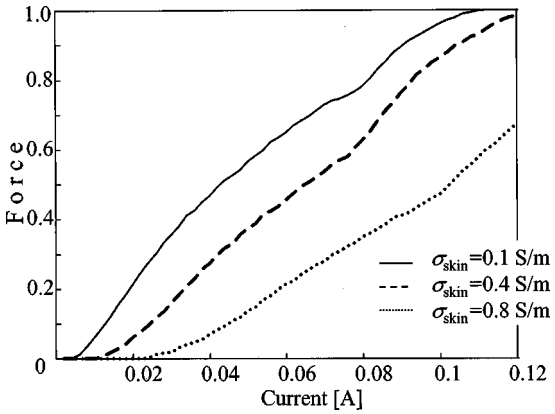

FIGURE 8. Influence of the conductivity of skin on the IRC (transcutaneous model).

slope than that of the surface stimulation IRC, due to the higher current density values resulting when intramuscular stimulation is used. An additional feature of the IRC in this case is the absence of an initial dead zone region, possibly because of the presence of singular values of the current density near the stimulation electrodes.

Figure 8 presents the IRC for the transcutaneous model for different values of conductivity of the skin layer σ_{skin}, while σ_{fat} and σ_{muscle} are held constant. An increase of σ_{skin} (leading to an increase in K_2) reduces both the current density in the muscle slice and the slope of the IRC. Irregularities in IRCs were due to the discretization along the *x* direction, as a result of the finite length of the fibers (50 mm).[8]

Parameter Estimation

The best fit to our experimental recruitment data during parameter estimation for a four-layer (air, skin, fat, muscle) surface stimulation model is achieved with the following parameters: $\sigma_{\text{skin}}=0.4$ S/m, $\sigma_{\text{fat}}=0.04$ S/m, and $\sigma_{\text{muscle}}=0.7$ S/m (the corresponding reflection coefficients are $K_2=0.81$ and $K_3=-0.89$); and the minimal current density midway between electrodes is 3.5 A/m^2. The conductivity values lie within the physiological,[7] and the current density correspond to previously published results.[32]

DISCUSSION

This study outlines an analytical model for the electric field distribution within an electrically activated muscle. The electric potential was expressed as image series and provides both an efficient alternative representation and a clear physical interpretation of the individual terms (i.e., properly weighted and shifted point-sources responses). Major factors affecting the potential distribution during surface stimulation are the nonuniform resistance of the skin (e.g., stratum corneum, epidermis, and dermis), fat, and muscle fascia. The derived model allows to calculate the electric field in configurations with several parallel tissue layers with arbitrarily placed electrodes, using relatively low computational power.

A basic assumption in the model is the stationarity of the current distribution, i.e., that the capacitive and inductive effects of the medium are sufficiently small. This is satisfied since the equilibrium potential is achieved within a time scale that is shorter than that of the action potential. The medium can thus be modeled as purely resistive and the field potential was assumed to satisfy the Laplace equation at each instant in time.[27] Air was modeled as a perfect insulator.

Anisotropy was not taken into account in this study. However, the nature of the solution in terms of an integral formulation for a transversely anisotropic stratified medium was indicated by Grant and West.[11] The image method has already been successfully applied to simple anisotropic geometries.[11,22] The implementation of the image method in more complex anisotropic multilayered media is, however, a crucially important research topic. The image method is a promising method for applications beyond those presented in this study. One example is to calculate the extracelluar potential distribution in a number of single-fiber models,[24,40] where the extracellular space is modeled as an infinite high-conductive medium. The image series, in conjunction with the method of moments[13] constitute an efficient computation scheme for a finite-size electrode or an array of electrodes in layered media.[23] Preliminary results show that, in surface stimulation, the recruitment model solutions for finite size and point electrodes compare well, except in the initial slope of the IRC, which was found higher in the finite compared to the point electrodes. In intramuscular stimulation the size difference between finite and point electrodes is much smaller, making the differences in the model solutions negligible. Thus, our closed-form solution can be used as a reference solution for future, more anatomically detailed description of the limb, based on MRI data[19] and using numerical solution techniques.

The presence of fat in the layer beneath the skin/electrode junction of the model has an interesting effect on the current densities in the whole medium. Under constant current conditions, fat prevents the lateral spread of current from the electrode, forcing the current to flow along the shortest path, i.e., across the thickness of the fat layer. On the other hand muscle tissue is a better conductor than fat, therefore allowing the current to spread laterally from the electrode. Carter *et al.*[2] reported that for a given total tissue thickness, patients with large amounts of subcutaneous fat would require a lower input current to maintain a given level of current density in a specific *z* layer, as compared to patients with little fat. This, however, was not confirmed in our results as shown in Fig. 6, because the skin layer has a higher conductivity than the fat layer and current pathways can close through the high-conductive skin layer without reaching the muscle layer.

The current density distribution obtained in the surface stimulation model was found to be largely nonuniform near the stimulating electrodes and was near uniform within a large part of the muscle volume. This may lead to fast fatiguing of the fibers adjacent to the stimulating electrodes, increase the threshold and make it more difficult to activate the middle portion of the muscle. Decreasing the interelectrode distance or using additional stimulation electrodes can, however, help both in making the current density more evenly distributed near the electrodes, preventing fast fatigue and decreasing the stimulation threshold midway between the electrodes.

The calculated IRC results demonstrated the influence of tissue conductivity on the maximum force value. The general IRC shape appeared sigmoidal, in agreement with previous results.[5,9,21] An additional expected result was that the intramuscular curves were shifted towards lower stimulus amplitude and had a higher slope when compared to surface IRC. The success in matching both the IRC experiments and IRC numerical simulation in a rather restricted value range of the parameters, demonstrate that our simplified planar model may be applied quite effectively in FES problems. An additional advantage in our model validation is that the given inputs were not arbitrarily assumed, but derived from the electric field distribution due to the stimulating electrodes. The skin conductivity as well as presence of fat or other low conductive tissue (e.g., muscle fascia) play a major role in demonstrating the difference in activation patterns between intramuscular and surface stimulation.

Experimental studies have shown that the location of the stimulating electrodes with respect to the motor points (MP)[39] can strongly affect the maximal force[10] and also reduce muscle fatigue. Thus, moving the electrodes away from the MPs results in: (a) reduction of the excitation force of the whole muscle; (b) a more continuous nature of recruitment; and (c) reduced slope of the IRC. The last two of these results are often desirable for FES controllability.

Muscle activation was related in our simplified macroscopic model validation to the current density. This was justified by the data used, i.e., pulse width 250 μs, combined thickness of skin and fat layers of about 1 cm, and electrode placement slightly away from the MPs to minimize fatigue. In the real situation, both mechanisms (electric field and its spatial derivative) may produce a muscle contraction. The question which mechanism is more dominant depends heavily on geometry, i.e., distances relative to the electrode of the nerve fibers, branching points and nerve endings.[31–33] Future models should clarify more precisely the borderlines determining which of the mechanisms is dominant for a given case. The location of fibers with different diameters within the nerve bundles[37] and information on the muscle fiber population and their force generation properties (slow versus fast) are also important but need further anatomical and physiological data.

The numerical simulations demonstrate the importance of an appropriate modeling of the tissue layers. Oversimplified models which use a reduced number of layers may result in an inaccurate simulation which greatly obscures the real FES situation. Since, our model can handle effectively problems with any number of the layers, the decision whether a particular layer should be included in the model can be accurately made.

Our simplified *macroscopic* model verification may have overlooked some of physiological details but is nevertheless advantageous in that it can provide an insight into practical FES applications. Particularly it demonstrates how the tissue's electrical properties influence the difference between intramuscular and surface stimulation.

ACKNOWLEDGMENT

This study was supported by the Segal Foundation.

NOMENCLATURE

Roman Symbols

$\mathbf{E}$	electric field intensity (V/m)
I	current (A)
J_0	Bessel function of zero order of the first kind
K	local reflection coefficient
P	observation point
$R(\lambda), T(\lambda)$	global reflection and transmission coefficients
S	source point
V	potential function (V)
h	thickness of a layer (m)
$\mathbf{j}$	current density (A/m^2)
n	number of layers
x,y,z	rectangular coordinates

Greek Symbols

λ	separation coefficient
σ	conductivity of layer (S/m)
δ	Dirac delta function

REFERENCES

[1] Carroll, S. G., R. J. Triolo, H. J. Chizeck, R. Kobetic, and R. Kobetic, and E. B. Marsolais. Tetanic responses of electrically stimulate paralyzed muscle at varying interpulse intervals. *IEEE Trans. Biomed. Eng.* 36:644–653, 1989.

[2] Carter, E., S. Pollack, and C. Brighton. Theoretical determination of the current density distribution in human vertebral bodies during electrical stimulation. *IEEE Trans. Biomed. Eng.* 37:606–615, 1990.

[3] Coburn, B.. Neural modeling in electrical stimulation. *Crit. Rev. Biomed. Eng.* 17:133–178, 1989.

[4] Crago, P. E., P. H. Peckham, J. T. Mortimer, and J. P. Van Der Meulen. The choice of pulse duration for chronic electrical stimulation via surface, nerve, and intramuscular Electrodes. *Ann. Biomed. Eng.* 2:252–264, 1974.

[5] Durfee, W. K., and K. E. MacLean. Methods for estimating isometric recruitment curves of electrically stimulated muscle. *IEEE Trans. Biomed. Eng.* 36:654–666, 1989.

[6] Einziger, P. D., L. Livshitz, and J. Mizrahi. Rigorous image series expansions of quasistatic Green's functions for regions with planar stratification. *IEEE Trans. Antennas Propag.* (submitted).

[7] Foster, K. R., and H. P. Schwan. Dielectrical properties of tissues. In: CRC Handbook of Biological Effects of Electro-

magnetic Field, edited by C. Polk and E. Postow. Boca Raton, FL: CRC Press, 1986, pp. 26–95.
[8] Friederich, J. A., and R. A. Brand. Muscle fiber architecture in the human lower limb. *J. Biomech.* 23:91–95, 1990.
[9] Gorman, P. H., and J. T. Mortimer. The effect of stimulus parameters on the recruitment characteristics of direct nerve stimulation. *IEEE Trans. Biomed. Eng.* 30:407–414, 1983.
[10] Grandjean, P. A., and J. T. Mortimer. Recruitment properties of monopolar and bipolar epimysial electrodes. *Ann. Biomed. Eng.* 14:53–66, 1986.
[11] Grant, F. S., and G. F. West. Interpretation Theory in Applied Geophysics. New York: McGraw-Hill, 1965, pp. 407–414.
[12] Grill, W. M.. Modeling the effects of electric fields on nerve fibers: Influence of tissue electrical properties. *IEEE Trans. Biomed. Eng.* 46:918–28, 1999.
[13] Harrington, R. F. *Field Computation by Moment Methods*. New York: Macmillan, 1968.
[14] Hause, H. A., and J. R. Melcher. Electromagnetic Field and Energy. Englewood Cliffs, NJ: Prentice-Hall, 1989.
[15] Hummel, J. N.. A theoretical study of apparent resistivity in surface potential methods.*Trans. Am. Inst. Min. Metall. Pet. Eng.*, 97:392–422, 1932.
[16] Jack, J. J. B., D. Noble, and R. W. Tsien. Electric Current Flow in Excitable Cells. Oxford: Claredon, 1988, pp. 99–129.
[17] Keller, G. V., and F. C. Frischknecht. Electrical Methods in Geophysical Prospecting. Oxford: Pergamon, 1970, pp. 90–145.
[18] Lagace, P. J., J. Fortin, and E. D. Grainic. Interpretation of resistivity sounding measurements in N-layer soil using electrostatic images. *IEEE Trans. Power Deliv.* 11:1349–1354, 1996.
[19] Levin O., J. Mizrahi, M. Gornish, E. Prishkulnik, A. Herskowitz, and E. Isakov. The effect of training by FES on geometry and force of paralyzed thigh muscle Proceedings of the 2nd Annual Conference of the International Functional Electrical Stimulation Society and the Fifth, Triennial Conference on Neural Prostheses: Motor System V. Burnaby British Columbia, Aug. 1997, pp. 19–20.
[20] Levin, O., and J. Mizrahi. EMG and metabolite-based prediction of force in paralyzed quadriceps muscle under interrupted stimulation. *IEEE Trans. Rehab. Eng.* 7:301–314, 1999.
[21] Levy, M., J. Mizrahi, and Z. Susak. Recruitment, force and fatigue characteristics of quadriceps muscles of paraplegics isometrically activated by surface functional electrical stimulation. *J. Biomed. Eng.* 12:150–156, 1990.
[22] Li, P., and N. F. Uren. Analytical solution for the point source potential in an anisotropic 3-D half-space. I. Two-horizontal-layer case. *Math. Comput. Modeling* 26:9–27, 1997.
[23] Livshitz, L. Einziger, P. D. Mizrahi. J. A model of finite electrodes in layered media: An hybrid image series and moment method scheme. Proceedings of the 22nd Annual International Conference of the IEEE Engineering in Medicine and Biology Society, Chicago, 2000 July 23–28.
[24] McNeal, D. R.. Analysis of model for excitation of myelinated nerve. *IEEE Trans. Biomed. Eng.* 23:329–337, 1976.
[25] Mizrahi, J., E. Isakov, and Z. Susak. Myoelectric and force characteristics in transcutaneous isometric FES. *Basic Appl. Myology*, 4:147–154, 1994.
[26] Minzly, J., J. Mizrahi, E. Isakov, Z. Susak, and M. Verbeke. Computer-controlled portable stimulator for paraplegic patients. *J. Biomed. Eng.* 15:333–338, 1993.
[27] Plonsey, R. Bioelectric Phenomena. New York: McGraw-Hill, 1969, pp. 129–139.
[28] Plonsey, R. Electrical field modeling. In: Neural Stimulation, edited by Myklebust, J. B., Cusick, J. F., Sances, A. J., and Larson S. J. Boca Raton, FL: CRC Press, 1985, pp. 13–32.
[29] Ranck, J. B.. Which elements are excited in electrical stimulation of mammalian central nervous system: A review. *Brain Res.* 98:417–440, 1975.
[30] Rattay, F. Electrical Nerve Stimulation. Wien: Springer, 1990.
[31] Reilly, J. P. Electrical Stimulation and Electropathology. Cambridge: Cambridge University Press, 1992, pp. 95–132.
[32] Reilly, J. P. Applied Bioelectricity. New York: Springer, 1998.
[33] Roth, B. J.. Mechanism for electrical stimulation of excitable tissue. *Crit. Rev. Biomed. Eng.* 22:253–305, 1994.
[34] Stefanesco, S., C. Schlumberger, and M. Schlumberger. The distribution of electrical potential about a point electrode in an earth of horizontal, homogeneous, and isotropic beds. *J. Phys. Radium* 1:130–141, 1930.
[35] Stegeman, D. F., J. P. C. de Weerd, and E. G. J. Eijkman. A volume conductor study of compound action potentials of nerves: The forward problem. *Biol. Cybern.* 33:97–111, 1979.
[36] Tikhonov, A. N. and A. A. Samarskii. Equations of Mathematical Physics. Oxford: Pergamon, 1963, pp. 427–433.
[37] Veltink, P. H., B. K. van Veen, J. J. Struijk, J. Holsheimer, and H. B. K. Boom. A modeling study of nerve fascicle stimulation. *IEEE Trans. Biomed. Eng.* 36:683–691, 1989.
[38] Wait, J. R. Geo-Electromagnetism. New York: Academic, 1982.
[39] Walthard, K. M., and M. Tchicaloff. Motor points. In: Electrodiagnosis and Electromyography, edited by E. Licht. New Haven, CT: C. Licht, 1971, pp. 153–170.
[40] Warman, E. N., W. M. Grill, and D. M. Durand. Modeling the effects of electric fields on nerve fibers: Determination of excitation thresholds. *IEEE Trans. Biomed. Eng.* 39:1244–1254, 1992.